Journal of Zhejiang University-SCIENCE A in press
www.jzus.zju.edu.cn; www.springer.com/journal/11582
E-mail: jzus_a@zju.edu.cn

Research Article
https://doi.org/10.1631/jzus.A2600046

Unsteady aerodynamic effects and underbody flow characteristics of high-speed trains at 400 km/h with bogie covering structures using an improved delayed detached-eddy simulation method

Hongkang LIU[1,2,3], Jinning GONG[2,3], Yatian ZHAO[1,2,3], Zhenyu ZHANG[6], Kehui PENG[2,3], Wenyue WANG[2,3], Tiantian WANG[2,4,5]✉

[1]*Extreme Flow Energy Frontier Science Centre, Central South University, Changsha 410075, China*
[2]*Key Laboratory of Traffic Safety on Track of Ministry of Education, School of Traffic & Transportation Engineering, Central South University, Changsha 410075, China*
[3]*National & Local Joint Engineering Research Centre of Safety Technology for Rail Vehicle, Central South University, Changsha 410075, China*
[4]*College of Mechanical and Vehicle Engineering, Hunan University, Changsha 410082, China*
[5]*College of Future Technology, Hunan University, Changsha 410082, China*
[6]*CRRC Qingdao Sifang Co., Ltd., Qingdao 266111, China*

Abstract: Although high-speed train (HST) bogie covers effectively reduce aerodynamic drag, they raise safety concerns due to lift-induced oscillations caused by unsteady underbody flow. This study investigates the effects of various bogie covering structures on aerodynamic load pulsations, pressure fluctuations, and underlying flow mechanisms in HSTs using an improved delayed detached-eddy simulation (IDDES) at 400 km/h. Three covering configurations are considered: fully enclosed covers (FECs), separated-type covers (STCs), and skirts-only. The numerical results show that all covering configurations significantly reduce the total aerodynamic drag. Specifically, FECs achieve the largest reduction at 19.81%, while STC and the skirt-only configurations achieve reductions of 16.24% and 14.45%, respectively. STCs perform better than FECs in suppressing lift fluctuations of car bodies, effectively reducing the root-mean-square (RMS) lift coefficient by up to 44%. While both STCs and FECs significantly attenuate pressure fluctuations by up to 98% in the head bogie cabins and 83% in the tail cabins, they intensify fluctuations in the middle cabins by 43% for STCs and 162% for FECs. Spectral analysis reveals that the dominant lift fluctuation frequencies for STCs and FECs primarily fall within 7–14 Hz, with a secondary range of 63–72 Hz. These fluctuations are attributed to cavity flow-induced resonance within the bogie cabin, which couples the internal and external airflows via the wheel gaps. Additionally, FECs exhibit higher fluctuation amplitudes than STCs. Furthermore, boundary layer instability on the lower surface of the head cover induces periodic high-frequency flow field fluctuations with a dominant frequency exceeding 115 Hz.

Key words: High-speed train; Bogie covers; Aerodynamic drag; Lift fluctuations; Pressure fluctuations; Underbody flow fields

1 Introduction

As the operating speeds of high-speed trains (HSTs) increase, their aerodynamic challenges have become more pronounced (Muñoz-Paniagua and García, 2020). Bogie encapsulation, an important and effective approach to drag reduction (Xia et al., 2016; Zhang et al., 2018; Dong et al., 2020), has been integrated into the aerodynamic drag reduction design of next-generation HSTs in China (Dai et al., 2024). However, such encapsulation significantly alters the underbody flow dynamics. Given the complexity of this flow regime, the resulting aerodynamic disturbances in the structure warrant thorough investigation.

Reducing aerodynamic drag and noise in HSTs has become a global research priority (Zhang et al., 2016; Guo et al., 2024). In academia, substantial progress has been made regarding the drag reduction efficacy of bogie enclosures (Zhang et al., 2018; Dong et al., 2020). Studies demonstrate that, compared to

✉ Tiantian WANG, wangtiantian@csu.edu.cn
Hongkang LIU, https://orcid.org/0000-0002-7534-1016
Tiantian WANG, https://orcid.org/0000-0003-0137-7881

Received Jan. 22, 2026; Revision accepted June 15, 2026; Crosschecked

fully exposed bogie arrangements, encapsulated configurations can achieve drag reduction rates exceeding 30% (Zhang et al., 2022) while also exhibiting superior aerodynamic performance under both crosswind and noncrosswind conditions. Additionally, installing skirts offers a feasible solution for mitigating wheel-generated noise (Zhang et al., 2019). In engineering practice, the dominant configurations primarily include skirt enclosures (Moon et al., 2014; Wang et al., 2020) and bogie cover enclosures (Dai et al., 2024); notably, skirt technology has matured and is widely implemented (Wang et al., 2019). Researchers worldwide have conducted extensive investigations into the aerodynamic performance of HSTs with various enclosure configurations. Moon et al. (2014) demonstrated that three skirt designs reduced the drag of the HEMU-430X six-car train by 7.8%. Li et al. (2025) numerically revealed that skirts optimize the pressure distribution on bogie cabin sidewalls, mitigating unsteady aerodynamic loads and resonance risks. Subsequent investigations by Wang et al. (2020), Shang et al. (2023), Zhang et al. (2022), and Dai et al. (2024) corroborated that sealing bogie cabins or installing bogie covers yields drag reduction rates ranging from 25.5% to 42%, while also improving the flow field and suppressing vortex shedding. However, while bogie covers contribute significantly to drag and noise reduction, they simultaneously introduce safety risks associated with flow-induced fluctuations (Baker, 2016). Within the underbody flow field, unsteady pressure fluctuations driven by vortices act directly on the bogies and covers. If the excitation frequency aligns with the natural frequency of the cover, it may trigger structural resonance, potentially leading to component detachment.

Prior studies regarding the underbody flow field have confirmed the flow complexity in the bogie region. Zheng et al. (2011) employed the delayed detached eddy simulation (DDES) method to identify high-turbulence unsteady flows, observing that multiscale vortex structures form as airflow passes over each bogie. Kwon (2023) noted that aerodynamic fluctuations in the underbody region are highly sensitive to variations in incoming flow. Liu et al. (2019) further verified that bogies serve as key sources of vortex and wake fluctuations, whose flow mechanisms warrant prioritized investigation. Additionally, Dong et al. (2022) observed strong shear layers within the cabin region, where shear instability coupled with complex bogie components exacerbates turbulence. He et al. (2024) highlighted that bogie components experience intense pressure fluctuations due to their location within the upstream separated shear layer, thereby acting as primary noise sources; the resulting noise spectrum exhibits broadband characteristics dominated by low frequencies. Research on the surface fluctuating pressure of HSTs has emerged relatively recently (Xiao et al., 2010). Due to the train's nonstreamlined geometry, surface roughness, and ground effects, a complex turbulent flow field forms around the vehicle, leading to vortex shedding, flow separation, and reattachment. These phenomena ultimately manifest as surface fluctuations on the car body (Li et al., 2025). Most existing studies have predominantly focused on key aerodynamic regions, such as the head and tail cars. Li et al. (2025) performed proper orthogonal decomposition (POD) analysis on the trailing car's surface pressure and found that positive and negative pressure fluctuations concentrate near the bogie skirt edges, directly influencing lateral aerodynamic vibrations. Xiao et al. (2010) and Wang et al. (2015) extracted the fluctuating pressure characteristics of the head car using large eddy simulation (LES), while Li et al. (2011) computed surface pressure fluctuations and flow field boundaries using various turbulence models to analyze their frequency-domain behaviors. Although these studies have laid a solid foundation for understanding surface pressure fluctuations, notable gaps remain regarding the underbody region, specifically the pressure fluctuation characteristics around bogie covers.

To date, the underlying mechanisms governing the pressure and lift fluctuations induced by bogie covers remain insufficiently explored. The literature offers fragmented insights, leaving a distinct gap in understanding the intrinsic correlation between these fluctuations and the complex underbody cavity flows (Gao et al., 2021). To address the aforementioned research gaps, this study conducts an in-depth investigation into the influence of bogie covers on train aerodynamic performance, systematically explores the characteristics of pressure and lift fluctuations acting on bogie covers, and reveals the intrinsic correlation between the lift fluctuation

characteristics of bogie covers and the underbody flow field of bogie cabins. The research findings can provide reliable theoretical support for the structural safety design of bogie covers and the optimization of train aerodynamic performance.

2 Methodology

2.1 Numerical method

This study uses the commercial software STAR-CCM+ for numerical simulations based on the finite volume method. Given the operating speed of the HST at 400 km/h (approximately 0.33 Mach), the flow is considered compressible (Zhou et al., 2020; Huang et al., 2024; Li et al., 2024). Furthermore, the improved delayed detached-eddy simulation (IDDES) and Coupled Fluid Solver are key tools for addressing high-Reynolds-number, strongly separated, unsteady, and compressible flows, and their combination can accurately capture transient vortex structures, pressure fluctuations, and dynamic characteristics of aerodynamic loads (Zhou et al., 2020). Therefore, this study employs the IDDES method based on the SST k-ω model and coupled fluid solver to obtain high-precision unsteady turbulent simulation results. Further details on the numerical solution are provided in Section S1 of the Electronic Supplementary Materials (ESM).

2.2 Computational models, computational domain and boundary conditions

In this study, 1:8 scaled models are adopted for the numerical simulations to ensure validation consistency, computational feasibility, and aerodynamic similarity. Specifically, this scale aligns with the physical benchmark model from the China Aerodynamics Research and Development Center (CARDC) wind tunnel tests (Li et al., 2023), guaranteeing a direct and rigorous validation of the numerical methodology. The flow fields around the scaled models enter the Reynolds number self-similarity regime, fundamentally ensuring the physical reliability of the aerodynamic evaluations.

The train consists of three cars: Car 1 (head car), Car 2 (middle car), and Car 3 (tail car), as shown in Fig. 1a. Mechanically, the head and tail cars are trailers with unpowered bogies, while the middle car is a powered car equipped with motorized bogies. Notably, the bogie covers are installed exclusively on unpowered bogies. The powered bogies are left uncovered because the internal high-power traction motors and gear transmission systems severely restrict the available installation space (Zhao et al., 2025). Furthermore, the covers obstruct the substantial cooling airflow required for heat dissipation during high-speed operation. It should be noted that all dimensions provided below are based on the 1:1 full-scale model. The total length of the train is 80.7 m, with the head and tail cars each measuring 27.5 m. The carbody width is 3.36 m, and the height is 4.05 m (defined as the characteristic length, H). The bogie model includes main components (wheelsets, frames, and brake calipers). Detailed dimensions are in Section S2 of the ESM.

Fig. 1b illustrates the four simulation cases: Case 0 without skirts or bogie covers; Case 1, featuring skirts on the head and tail cars; Case 2, with separated-type covers (STCs) and skirts; and Case 3, with fully enclosed covers (FECs) and skirts. The STC configuration uses axle-mounted brake discs with covers attached to the bogie frame, introducing numerous opening clearances (e.g., front/rear walls, lateral sides, and wheel rims). Conversely, the FEC configuration employs wheel-mounted brake discs with covers anchored directly to the car body. Featuring only minimal gaps near the train nose and gap-free boundaries elsewhere, FEC restricts airflow exchange primarily to the wheel rim openings, thereby achieving significantly enhanced sealing performance over STC.

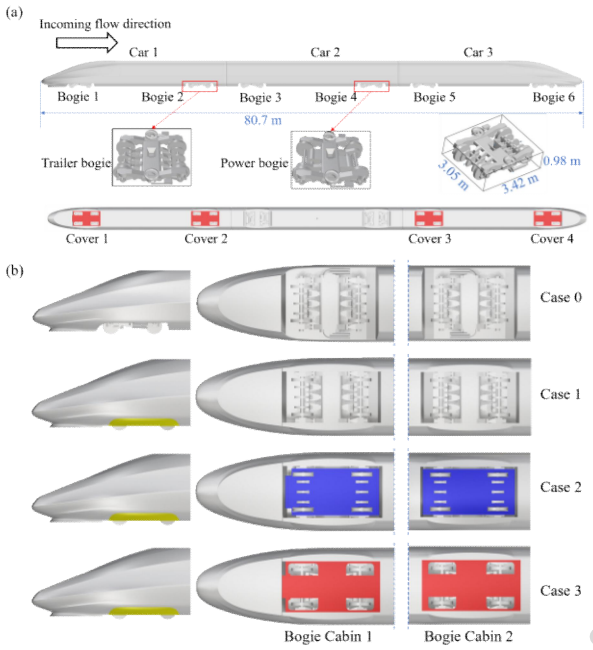

Fig. 1 Geometry models: (a) Sketch of the high-speed train model; (b) HST models of all cases

The computational domain and boundary conditions are illustrated in Fig. 2. With the train height H defined as the characteristic length, the domain extends 15H upstream from the train nose and 35H downstream from the tail. This longitudinal span ensures that the outlet boundary is sufficiently remote to prevent boundary reflection effects from contaminating the near-wake flow. At the inlet, a uniform free-stream velocity of (111.11, 0, 0) m/s was imposed, corresponding to a cruising speed of 400 km/h. The inlet turbulence intensity and turbulent viscosity ratio were set to 1% and 10, respectively. Although the CARDC wind tunnel (Li et al., 2023) exhibits a turbulence intensity below 0.12%, a 1% intensity was employed in the simulation to prevent nonphysical decay of turbulent viscosity in the far field and to ensure robust numerical convergence of the IDDES solver. The fluid properties are detailed in Section S3 of the ESM. To account for the ground effect, the ground and tracks were designated as moving no-slip walls, with their velocity and direction matching the incoming flow.

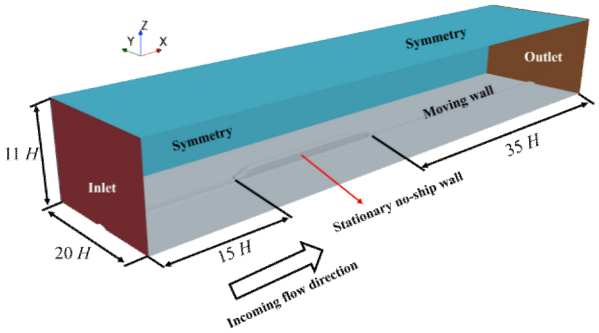

Fig. 2 Computational domain and boundary condition

2.3 Computational mesh and validation

The computational domain is spatially discretized using a Cartesian cut-cell mesh generated in STAR-CCM+, with consistent meshing protocols applied across all cases. To satisfy the requirements of the IDDES method, the wall-normal spacing of the first prismatic layer was set to 5×10^{-5} m, maintaining $y^+ \approx 1$. The details of the grid setup and the computational mesh topology can be found in Section S4 and Fig. S1 of the ESM. To systematically evaluate the aerodynamic performance of the high-speed train, the aerodynamic drag coefficient (C_d), lift coefficient (C_l), and surface pressure coefficient (C_p) are introduced as dimensionless parameters, which are defined in Section S4, Eqs. (S1)–(S3) of the ESM. To validate grid independence, three sets of meshes with varying resolutions (coarse, medium, and fine) were evaluated. The specific mesh density parameters and calculations are provided in Table S1 in Section S4 of the ESM. Notably, the difference in the total C_d between the medium and fine meshes is only -2.53%. In contrast, the coarse mesh shows a significantly larger deviation of -5.68% compared to the fine mesh. Therefore, the medium mesh meets the accuracy requirements for simulating the HST flow field. To balance computational cost and accuracy, the medium mesh is selected for all subsequent simulations.

The proposed numerical method is validated against wind tunnel test data (Li et al., 2023) obtained from a large low-speed wind tunnel at the CARDC. The test employed a 1:8 scale train model (consisting of a head car and a half-length car body). Section S5 and Fig. S2 of the ESM present the wind tunnel test setup details for numerical validation and the corresponding geometric comparison between the numerical and experimental models. Validation

focused on two primary aerodynamic observables: the C_d of the head car and the C_p distribution along the longitudinal streamlined centerline. Table 1 presents the head car C_d derived from both the wind tunnel test and the numerical simulation. The results indicate that the simulated drag coefficient deviates by -3.39% from the wind tunnel data, which is within the standard error margin of 5%. Additionally, Fig. 3 compares the surface pressure tap measurements on the leading car with the numerical predictions. The close match between the simulated surface pressures and the experimental data validates the predictive accuracy of the numerical method regarding car body surface loads.

Table 1 Comparison of the aerodynamic drag coefficient for the numerical simulation and wind tunnel test (Li et al., 2023)

/	C_d value of the head car
Wind tunnel test	0.118
Numerical simulation	0.122
Error	-3.39%

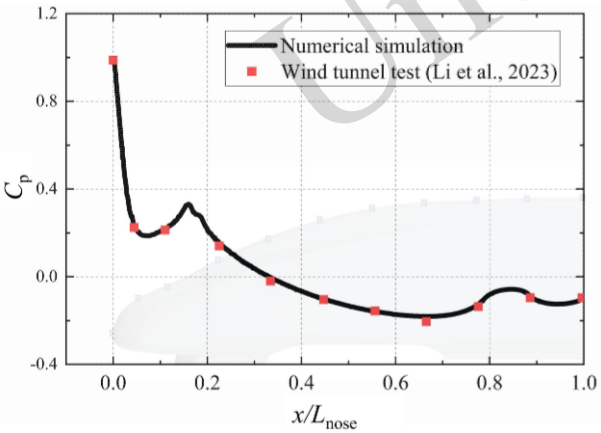

Fig. 3 Comparison of the surface pressure coefficient distributions between numerical simulation and wind tunnel test (Li et al., 2023)

For validation, comparisons are made with moving model tests (Bell et al., 2015) conducted at Reynolds numbers of 2.5×10^5 and 3.3×10^5. The mean underbody flow velocity ($U_{slipstream}$) at a specific track-side monitoring point (3 m from the track centerline and 0.2 m above the top of rail) is quantitatively compared with corresponding measurements from the moving model tests. The mathematical formulation for $U_{slipstream}$ is provided in Eq. (S4), Section S6 of the ESM. Notably, as illustrated in Fig. 4, the comparison reveals a high degree of consistency between the numerical results and the experimental data. Slight deviations are likely due to unavoidable geometric differences and specific model setup details that are not fully detailed in the literature. Overall, these results confirm that the numerical method employed in this study provides reliable predictions of the undertrain flow field.

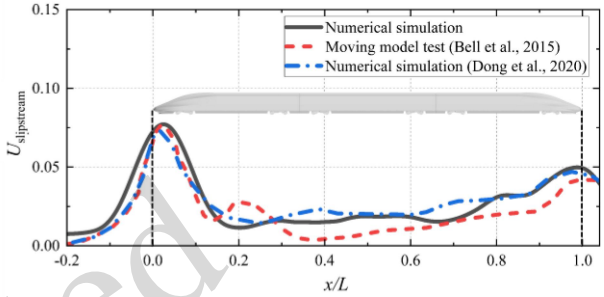

Fig. 4 Comparison of the present results with moving model experiments and prior numerical studies (Bell et al., 2015; Dong et al., 2020)

3 Results and discussion

3.1 Aerodynamic force

3.1.1 Aerodynamic drag force

This section compares the aerodynamic drag of trains with different bogie covering configurations. Table 2 presents the C_d values for various cases to evaluate the drag reduction performance of bogie encapsulations. First, compared to the baseline (Case 0), the total C_d is significantly reduced in all cases with skirts or covers, achieving reduction rates of 14.45%, 16.24%, and 19.81% for Cases 1, 2, and 3, respectively. Second, while adding skirts reduces drag for every car, the addition of covers further enhances drag reduction for the head and tail cars, with Case 3 achieving the maximum reduction. In contrast, the middle car shows the opposite trend: its C_d value in Cases 2 and 3 is higher than that in Cases 0 and 1, with Case 3 showing the most significant increase.

Table 2 Comparison of the aerodynamic drag coefficients of each car

\	Car 1	Car 2	Car 3	Total
Case 0	0.1230	0.0694	0.1079	0.3003
Case 1	0.0994	0.0620	0.0955	0.2569

Case 2	0.0907	0.0712	0.0897	0.2515
Case 3	0.0848	0.0728	0.0831	0.2408

Fig. 5 depicts the streamwise velocity distributions along the underbody longitudinal centerline (0.15 m below the underbody surface). Cases 2 and 3 exhibit markedly higher flow velocities than Cases 0 and 1, with Case 3 displaying the most substantial acceleration, particularly in the Car 2 region. Physically, this phenomenon is attributed to the streamlining effect of the bogie covers. By smoothing the geometric profile, the covers mitigate the momentum loss of the high-speed underbody flow. Consequently, this preserved high-momentum fluid impinges more aggressively upon the downstream bogie cabins of Car 2, directly resulting in increased aerodynamic drag for the middle car.

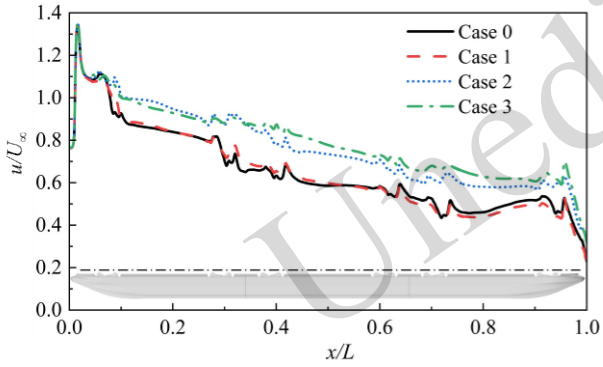

Fig. 5 Distribution of flow velocity along the longitudinal centerline of the underbody

3.1.2 Aerodynamic lift force

This section analyzes the aerodynamic lift of trains with different bogie covering configurations. Table 3 presents a comparison of C_l values for individual cars and the entire train. Car 1 exhibits downforce, while Cars 2 and 3 experience positive lift. Specifically, Car 3 displays the largest absolute value of C_l, while Car 2 shows the smallest. This trend is attributed to the varying flow fields: Car 1 is influenced by the stagnation pressure at the nose, while Car 3 is affected by flow separation in the wake region. Both conditions contribute to higher aerodynamic loads. In contrast, Car 2 is shielded by the upstream car, resulting in a smoother flow field and reduced lift. In terms of safety, the installation of STCs and FECs reduces the lift coefficient of Car 3 by 15% and 7%, respectively, compared to Case 0. Overall, the bogie covers effectively enhance the train's aerodynamic stability.

Table 3 Comparison of the aerodynamic lift coefficients of each car

/	Car 1	Car 2	Car 3	Total
Case 0	-0.0640	0.0023	0.0938	0.0321
Case 1	-0.0540	0.0149	0.0982	0.0591
Case 2	-0.0868	0.0144	0.0797	0.0072
Case 3	-0.0801	0.0254	0.0874	0.0327

Fig. 6 illustrates the root-mean-square (RMS) of the lift coefficients ($C_{l,rms}$) for the carbodies across the four configurations. Installing skirts alone slightly amplifies the lift fluctuations on the head and tail cars while offering minor attenuation for the middle car. In contrast, bogie covers universally reduce the unsteady loads on all cars. Notably, the STCs demonstrate superior suppression effectiveness compared to the FECs. Specifically, STCs reduce the $C_{l,rms}$ values by 41%, 30%, and 44% for the head, middle, and tail cars, respectively, outperforming FECs, which achieve reductions of 31%, 26%, and 37%.

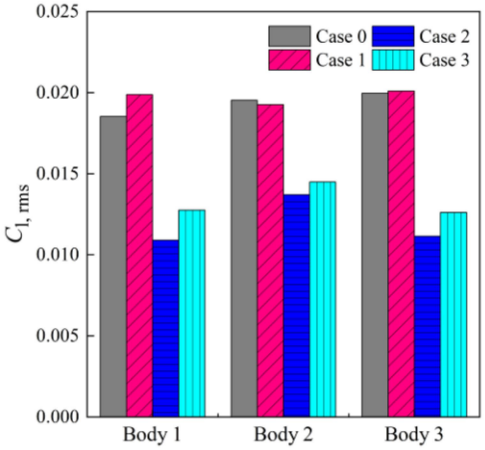

Fig. 6 RMS of the lift coefficients for car bodies

Fig. 7 presents the time-history curves of the C_l values for the individual bogie covers. After $t = 0.5$ s, the flow field fully develops and reaches a statistically stationary state characterized by stable periodic oscillations. Therefore, to eliminate initial numerical transients, only the stable temporal data from $t = 0.5$ s to 1.0 s are extracted for all subsequent time-averaged and unsteady aerodynamic analyses. Comparing the

two configurations, the STCs predominantly exhibit positive or near-zero mean lift values. In contrast, the FECs show a pronounced downward shift toward downforce, particularly for Covers 2, 3 and 4. Regarding transient fluctuations, the FECs demonstrate significantly more intense aerodynamic oscillations than the STCs. This instability is visually evident from the broader fluctuation bands in Fig. 7b.

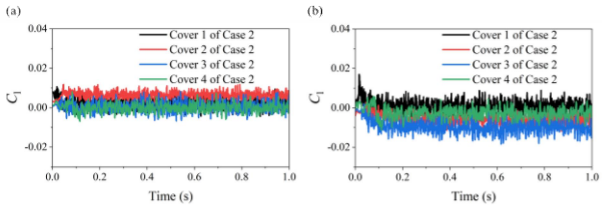

Fig. 7 Time-history curves of the lift coefficients for the bogie covers: (a) STCs in Case 2; (b) FECs in Case 3

Table 4 compares the lift characteristics of the covers in Case 2 and Case 3 to quantify their fluctuation properties. First, regarding the mean force, most covers in Case 2 experience positive lift, while those in Case 3 exhibit negative lift. Second, the RMS of the lift coefficients for STCs is consistently lower than that for FECs, indicating weaker aerodynamic instability. Specifically, comparing Case 2 to Case 3, the RMS values for Covers 1 through 4 are reduced by 22%, 17%, 14%, and 13%, respectively. Third, the fluctuation intensity follows a consistent order: Cover 3 > Cover 1 > Cover 4 > Cover 2. Additionally, regarding fluctuation amplitude, Covers 1 and 3 demonstrate the largest peak magnitudes among the four covers.

Table 4 Comparison of time-averaged lift coefficients, lift coefficients RMS, and maximum oscillation amplitudes for the bogie covers

	Time-averaged lift coefficients ($\times10^{-4}$)		RMS of the lift coefficients ($\times10^{-4}$)		Maximum fluctuation Amplitudes ($\times10^{-4}$)	
Type	STC	FEC	STC	FEC	STC	FEC
Cover 1	22	5	21	27	73	95
Cover 2	64	-62	15	18	61	57
Cover 3	5	-101	25	29	77	86
Cover 4	0	-26	21	24	73	71

The bogie cabin exhibits structural characteristics typical of a cavity. Thus, the underbody flow field near the cabin can be modeled as cavity flow for dynamic analysis. A boundary layer forms near the leading edge and separates as the airflow passes over the opening. Subsequently, the intense shear between the high-speed external flow and the internal cavity flow leads to the formation of a shear layer. This layer undergoes instability and oscillation, generating and transporting shed vortices downstream. When this vortex-laden flow impinges on the trailing edge, it triggers intense pressure fluctuations and noise. The classical method for predicting the modal frequencies of such flow-induced oscillations is the Rossiter semiempirical formula (Rossiter, 1962). Heller et al. (1971) subsequently refined this model to account for compressibility effects. The Heller-modified Rossiter formulations are detailed in Section S7, Eqs. (S5)–(S6) of the ESM. It is important to note that the Heller-modified Rossiter formula is primarily valid within the Mach range of 0.3–1.4; beyond this regime, the predictive accuracy deteriorates significantly.

As illustrated in Fig. 5, the incoming flow velocity at the underbody Bogie Cabin 1 of the head car is taken as $1.1U_\infty$, corresponding to 122.22 m/s. Calculations based on the semiempirical formula yield the following dominant excitation frequencies for Bogie 1: 10 Hz (1st mode), 23 Hz (2nd mode), 50 Hz (4th mode), and 64 Hz (5th mode). In contrast, the local Mach numbers at the underbody of the middle and tail cars remain below 0.3. Consequently, these regions fall outside the validity range of the Heller-modified Rossiter formula, precluding its application for these downstream bogie cabins.

To identify the frequency characteristics of the lift fluctuations, fast Fourier transform (FFT) analysis is performed on the lift coefficients of each car body and bogie cover. Fig. 8 presents the power spectral density (PSD) of lift coefficients. As observed in Fig. 8a–c, the dominant frequencies for all car bodies fall within the ranges of 7–10 Hz and 62–67 Hz, with a slight decrease observed from the leading to the trailing cars. Additionally, the PSD values for the head car are consistently higher than those for the tail car. Notably, Case 2 and Case 3 show comparable PSD levels, which are significantly suppressed compared to Case 0 and Case 1. This result confirms that the installation of covers significantly reduces the fluctuation energy for the head and tail cars.

Conversely, the PSD profiles of the middle car exhibit minimal variation across the four cases.

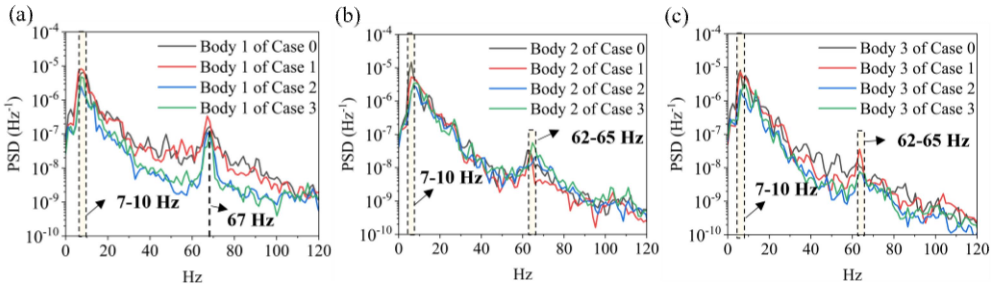

Fig. 8 PSD of lift coefficients for each car body: (a) Body 1; (b) Body 2; (c) Body 3

Fig. 9 compares the PSD of lift coefficients for STCs and FECs. The dominant frequencies for the bogie covers fall within the ranges of 7–14 Hz and 63–72 Hz. These frequencies correspond to those of the car bodies, indicating that both components are subjected to periodic forcing from the same dominant vortices. Comparisons show that the PSD values for FECs are consistently higher than those for STCs, reflecting more intense lift fluctuations in the FEC configuration. Furthermore, in the frequency range up to 30 Hz, the PSD values for Covers 3 and 4 are consistently higher than those for Covers 1 and 2. In contrast, for frequencies exceeding 30 Hz, Covers 1 and 2 surpass Covers 3 and 4. This observation suggests that the covers installed on the head car exhibit a higher dominant frequency range compared to those on the tail car. From this, it can be deduced that the dominant vortices around the head car oscillate at higher frequencies than those at the tail car.

The observed primary and secondary lift frequencies for the head car and its bogie covers align closely with the 1st- and 5th-order modes predicted by the semiempirical formula. This spectral agreement corroborates that cavity flow-induced resonance within the bogie region is the dominant aerodynamic excitation mechanism driving the periodic lift fluctuations. In contrast, for the middle and tail cars, the reduced underbody flow velocity results in a local Mach number below the validity range of the semiempirical formula, precluding theoretical prediction. However, as illustrated in Fig. 8 and Fig. 9, their dominant fluctuation frequencies exhibit slight deviations from those of the leading car. This frequency shift is attributed to the altered underbody flow conditions experienced by the downstream cars.

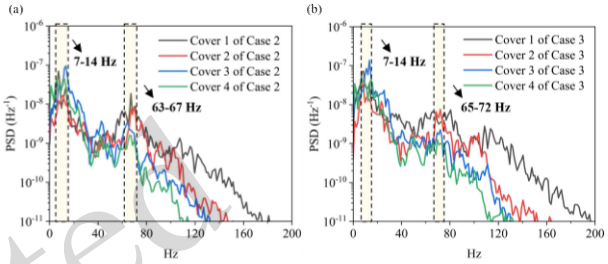

Fig. 9 PSD of lift coefficients for various covers: (a) Case 2; (b) Case 3

3.2 Analysis of flow field characteristics

3.2.1 Flow field of the underbody of the bogie covers

This section analyzes the unsteady flow field characteristics at the underbody of the bogie cabins for trains with different bogie covering configurations and establishes the correlation between the underbody flow field and the unsteady aerodynamic loads of the train. To investigate the effect of the covers on airflow exchange within the bogie cabin, Fig. 10 compares the time-averaged z-direction velocity distributions between Case 2 and Case 3. The airflow exchange paths vary significantly by configuration. For STC 1, airflow enters through the gap at the rear wall and exits via the front and side gaps. For STCs 2–4, inflow occurs through gaps at both the front and rear walls, as well as the wheel rim clearances, while outflow takes place through the sidewall tail gaps. For the FECs, Covers 1 and 4 possess small gaps near the cabin walls, while Covers 2 and 3 are virtually gap-free; thus, exchange relies primarily on the wheel gaps. Specifically, for Cover 1, airflow enters through the rear wheel gaps and exits via the front, whereas for Covers 2–4, the direction is opposite (entering front, exiting rear). Overall, STCs feature more openings, resulting in complex flow paths and a higher exchange rate. Conversely, FECs rely mainly

on wheel gaps, providing better sealing performance and significantly reducing the airflow exchange capacity.

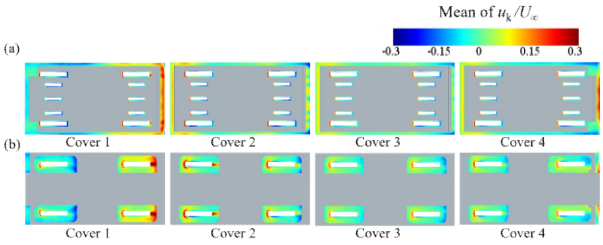

Fig. 10 Z-sectional velocity distributions of different covers: (a) STCs; (b) FECs

Fig. 11 presents the instantaneous velocity distributions near the lower surfaces of Covers 1 and 3. Cover 1 has sharp velocity gradients on the lower surface sides, easily inducing small-scale turbulent vortices, intensifying local velocity fluctuations, and causing strong surface pressure fluctuations. Its large front separation zone offers an unstable vortex generation environment; frequent vortex generation and shedding induce abrupt velocity changes, leading to high pressure fluctuation amplitude and frequency. STC 1, with side gaps, has sharper velocity gradients and stronger turbulent fluctuations, but its front, blocked by the brake disc, has weaker mid-section velocity gradients and turbulent fluctuations than those of FEC 1.

Cover 3 has a more uniform flow field, smaller separation zone, and lower transient vortex generation frequency. With gentle side velocity gradients, its large-scale vortices are more stable with limited energy transfer to smaller scales, and pressure fluctuations are significantly weaker than Cover 1. STC 3 shows downstream flow deceleration, and its side velocity gradients match those of FEC 3; moreover, its mid-section, blocked by the brake disc, also presents weaker velocity gradients and turbulent fluctuations than those identified in FEC 3.

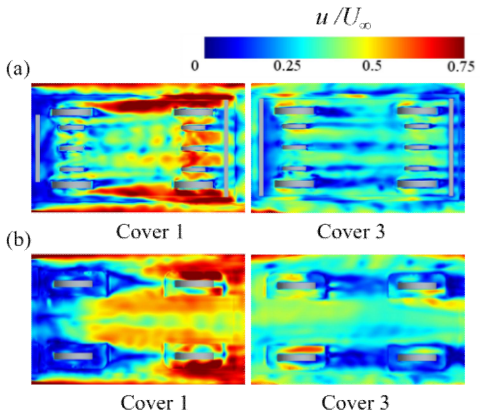

Fig. 11 Instantaneous velocity distributions near the lower surfaces of Cover 1 and Cover 3: (a) STCs; (b) FECs

Fig. 12 presents the velocity distribution characteristics along the longitudinal centerline of Bogie Cabin 1. When the high-speed incoming flow impinges on the obstacle catcher at the head of the train, the airflow is separated; as the airflow bypasses the front end of the obstacle catcher and continues to flow along its surface, the velocity gradually increases and reaches a stable state at the terminal region of the obstacle catcher surface. The high-speed airflow flowing along the obstacle catcher generates shear layer separation at the leading edge of Bogie Cabin 1. For Cases 0 and 1, since the bogie cabin is in a fully open state, the instability degree of the separated shear layer is the most intense, whereas in Cases 2 and 3, the sealing effect of the cover on the bogie cabin reduces the instability degree of the separated shear layer while inducing periodic flow pulsations in the middle region of the cover.

From Fig. 12 c–d, it can be observed that the spacings between periodic velocity pulsation peaks in the flow field on the lower surface of the middle region of the STC and FEC are 0.006L and 0.0065L, respectively. The local mainstream velocity is approximated by the line integral average of the streamwise velocity along the normal path (perpendicular to the streamwise x-direction) within the vortex region. The integration range is defined as extending from the maximum velocity point to the boundary on the lower surface of the cover where the velocity decays to 0. The corresponding integration formula is given as follows:

$$\overline{u}_{\text{local}} = \frac{1}{s}\int_0^s u(z)\mathrm{d}z, \tag{1}$$

where $\overline{u}_{\text{local}}$ denotes the approximated local

mainstream velocity, S represents the actual physical length of the normal integration path, and $u(z)$ denotes the streamwise velocity distribution along the z-axis. The flow pulsation frequencies of the middle region on the lower surface of the STC and FEC are calculated via Equation (2):

$$f = \frac{U_c}{\lambda}, \tag{2}$$

where f denotes the dominant frequency of flow velocity pulsation. U_c represents the vortex convection velocity, which is approximated in this study by the local mainstream velocity $\overline{u}_{local}$ in the vortex region on the lower surface of the cover. λ denotes the actual spatial spacing between adjacent velocity pulsation peaks. The local mainstream velocities $\overline{u}_{local}$ in the vortex regions on the lower surface of the STC and FEC are obtained via integration as 59 m/s and 62 m/s, respectively. Using Equation (2), the approximated dominant flow pulsation frequencies in the central region of the lower surface of STC and FEC are calculated to be 121 Hz and 118 Hz, respectively.

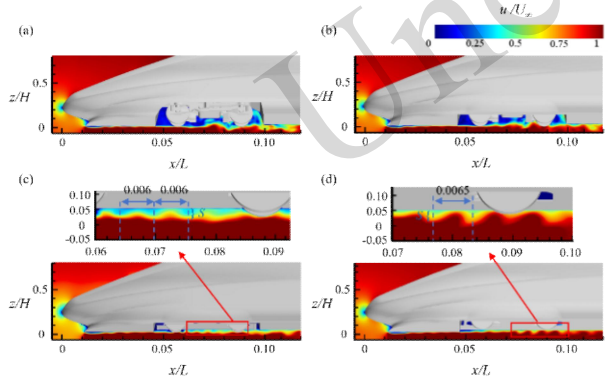

Fig. 12 Instantaneous velocity field near the underbody of Bogie 1: (a) Case 0; (b) Case 1; (c) Case 2; (d) Case 3; *L*: characteristic train length; *H*: characteristic train height

Fig. 13 illustrates the instantaneous vorticity distribution at the longitudinal centerline of Bogie Cabin 1 and along the wheel side, as well as the pressure distribution on the lower surface of Cover 1. Due to the fully open state of the bogie cavity in Case 0 and Case 1, a large-scale separated shear layer forms within the cavity. The instability of this layer generates large shedding vortices, which rapidly breakdown into small-scale vortices after impact, leading to highly disordered turbulence. Conversely, in Case 2 and Case 3, a relatively stable boundary layer forms on the central lower surface of the covers. Instability within this boundary layer induces periodic fluctuations, giving rise to high-frequency pressure fluctuations underneath the cover.

For the flow field on the wheel side, the incoming boundary layer is disrupted by the blocking effect of the wheels, forming a local stagnation zone with positive pressure on the windward side. As the flow bypasses the wheels, separation occurs due to the curvature of the wheel surfaces, generating separated vortices and a large negative pressure region. Afterward, the flow impinges on the rear edge of the covers, creating a local positive pressure zone. From Fig. 13 c–d, it can be observed that both the area and magnitude of positive and negative pressures in the wheel-side region of the cover surface are significantly larger than those in the central region. This phenomenon indicates that the vortices on the wheel side play a dominant role in the lift fluctuation of the covers.

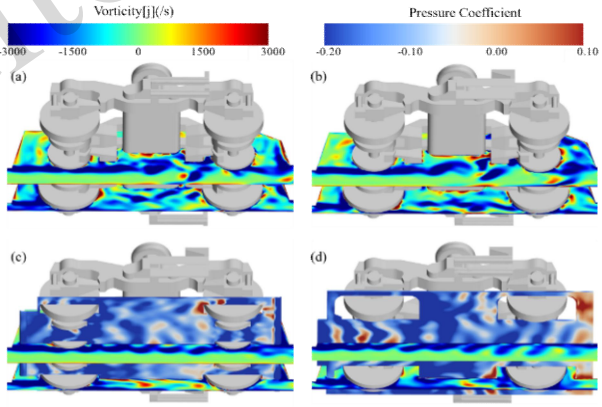

Fig. 13 Instantaneous vorticity distribution in the underbody region of Bogie 1 and pressure coefficient distribution on the lower surface of Cover: (a) Case 0 (b) Case 1; (c) Case 2; (d) Case 3

3.2.2 Pressure distribution characteristics of the bogie cabins

This section analyzes the pressure fluctuation characteristics inside the bogie cabins of trains with different bogie covering configurations. Fig. 14 compares the RMS values on the lower surfaces of the covers between Case 2 and Case 3. Overall, the pressure fluctuation intensity exhibits a decreasing trend along the longitudinal direction, consistent with the deceleration of the underbody flow. Most areas on the lower surface of Cover 1 have RMS values exceeding 0.05, while the corresponding areas on the other three covers generally range from 0.03 to 0.05.

For the STCs, regions with intense pressure fluctuations on the lower surfaces are located near the opening gaps, with an overall scattered distribution. These opening gaps serve as the exchange areas for airflow between the underbody and the interiors of the bogie cabins. In contrast, for the FECs, regions with intense pressure fluctuations on the lower surfaces are concentrated near the leading edges, both sides of the covers, and the wheel opening gaps, presenting a more centralized overall distribution.

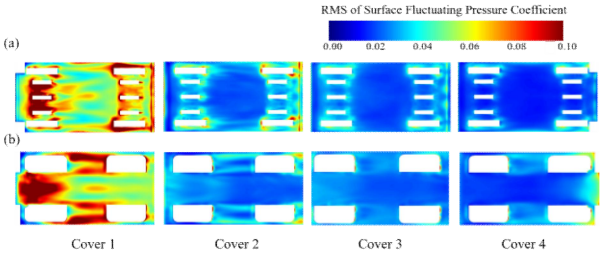

Fig. 14 Distribution of the RMS fluctuating pressure coefficients on the lower surfaces of the covers: (a) STCs; (b) FECs

As illustrated in Fig. 15, pressure measurement points are deployed at both lateral sides and the central region of the lower surface of the bogie cover, and FFT analysis was subsequently conducted on the acquired pressure measurement data. Fig. 16 illustrates the PSD of pressure fluctuations at the relevant measurement points on Cover 1. Surface points 1 and 3, adjacent to the wheel gaps, show dominant frequencies in the range of 5–13 Hz, which are consistent with the dominant frequency of the lift fluctuations. Conversely, points away from the wheel gaps on the lateral side exhibit a dominant frequency of approximately 65 Hz, matching the secondary frequency of the lift fluctuations. Furthermore, the dominant frequency at the central measurement point reaches 115 Hz. The excitation source for this frequency stems from periodic flow field fluctuations induced by boundary layer instability in the central region. Based on this comprehensive analysis, it is inferred that the dominant frequency of the lift fluctuations of the bogie cover is primarily driven by pressure fluctuations in the wheel gap region. Essentially, these fluctuations are a direct result of the periodic evolution of separated vortices at the wheel rim.

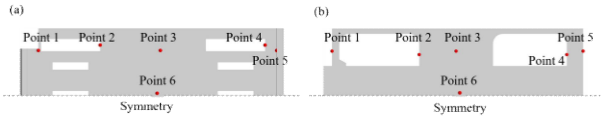

Fig. 15 Arrangement of pressure measurement points on the cover: (a) STC; (b) FEC

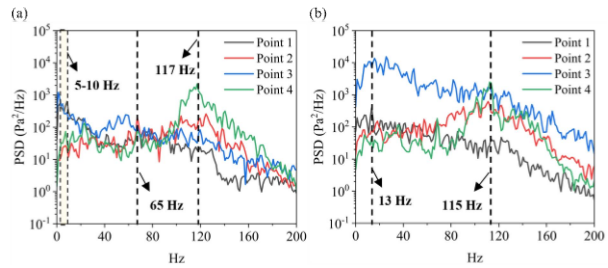

Fig. 16 PSD of fluctuating pressure on the surface of Cover 1: (a) STC; (b) FEC

To investigate the pressure fluctuation characteristics within the bogie cabins, pressure measurement points were arranged along the longitudinal centerline on the front walls of the cabins, the center of the bogie's lower surface, and the rear walls of the cabins, as illustrated in Fig. 17.

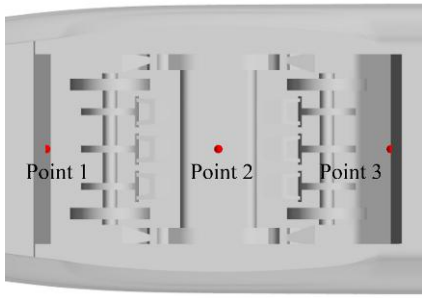

Fig. 17 Arrangement of pressure measurement points within the bogie cabins

Fig. 18 presents the PSD of pressure fluctuations at the internal measurement points of Bogie Cabin 1. The internal pressure fluctuations exhibit distinct dominant frequencies corresponding to cavity flow-induced resonance, namely, the first-order dominant frequency in the range of 7–10 Hz, the second-order dominant frequency of 20–23 Hz, the third-order dominant frequency of 38–40 Hz, the fourth-order dominant frequency of 50–53 Hz, and the fifth-order dominant frequency spanning 60–65 Hz. The first-order and fifth-order dominant frequency characteristics exhibit consistency with the dominant frequencies of the car body and cover lift fluctuations. The wheel gap opening on the bogie cover acts as the core channel for airflow exchange between the interior and exterior of the bogie cabin,

and the dominant frequency of pressure pulsations at this opening is highly consistent with the frequency of the cavity flow-induced resonance mode of the bogie cabin. In summary, the analysis indicates that cavity flow-induced resonance couples the internal and external flows via the wheel gaps, thereby dominating the lift fluctuations of the covers and car body.

To systematically evaluate the pressure fluctuation characteristics across the underbody, the PSD distributions for all six bogie cabins are analyzed. For brevity, the detailed spectral plots and comprehensive analyses are provided in Section S8 and Fig. S3 of the ESM. The spectral data exhibit dominant frequencies (specifically at 5–10, 50, and 65 Hz) that strictly correlate with cavity flow-induced resonance modes. Macroscopically, while bogie covers effectively attenuate pulsation energy in the head and tail cars, they amplify it in the middle car. Furthermore, the STC configuration, owing to its structural gaps, induces larger airflow exchange and higher pulsation energy in the head and tail cars, whereas the FEC exhibits a stronger flow-guiding effect that significantly amplifies fluctuations in the middle car.

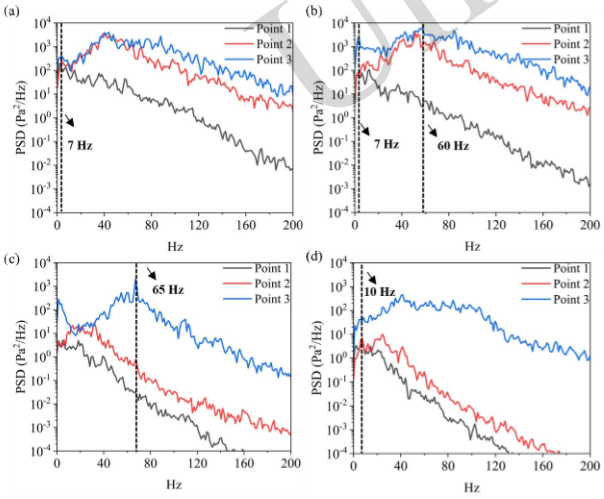

Fig. 18 PSD of pressure fluctuations in Bogie Cabin 1: (a) Case 0; (b) Case 1; (c) Case 2; (d) Case 3

To investigate the effect of bogie covers on pressure fluctuations in the underbody region, measurement points are arranged at the geometric center of the lower surface of the covers in Cases 2 and 3. The layout corresponds to Point 6 in Fig. 15. Corresponding measurement points are also installed for Cases 0 and 1. The collected data are analyzed using FFT, and the obtained PSD plots are presented in Fig. 19. For the underbody flow field of Bogie Cabin 1, the installation of the bogie cover reduces the oscillation energy of pressure fluctuations while increasing the dominant frequency. However, the instability of the boundary layer on the lower surface of the bogie cover induces periodic high-frequency flow field pulsations with a dominant frequency of approximately 115 Hz, which is in close agreement with the previously estimated dominant frequency. In contrast, for the underbody flow at the tail car's bogie cabins, the underbody flow velocity is relatively low, and the flow field has evolved into fully developed turbulence, leading to a negligible effect of the bogie cover installation on the dominant frequency of the underbody flow field pulsations.

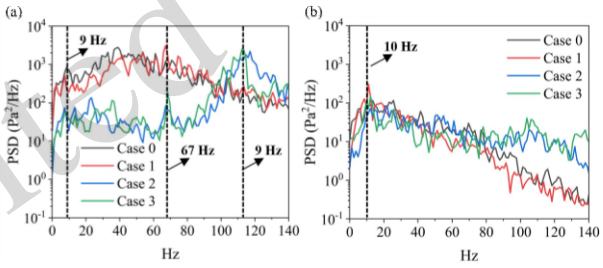

Fig. 19 PSD of pressure fluctuations in the underbody region of the bogie cabins: (a) Cabin 1; (b) Cabin 5

To elucidate the aerodynamic impact of skirts and covers on internal pressure fluctuations, Fig. 20 compares the RMS values across different cases. The arrangement of the measurement points is illustrated in Fig. 17. The results indicate that the bogie enclosure significantly influences the pressure distribution, with the rear wall of the bogie cabin typically exhibiting the most intense fluctuations. For Cases 0 and 1, the underbody airflow directly impacts the rear wall of Cabin 1, resulting in RMS values exceeding 0.14. The installation of STCs and FECs significantly suppresses pressure fluctuations inside the bogie cabins of the head and tail cars, with the most prominent reduction observed in Bogie Cabin 1 of the head car. Compared to Case 0, both cover configurations achieve a maximum reduction rate of 98% for the head car cabins and 83% for the tail car cabins. In contrast, the installation of covers mitigates the momentum loss of the high-speed underbody flow reaching the middle car, thereby increasing the fluctuation intensity. This increase is most prominent at the rear wall of Cabin 3, where the fluctuation levels for STCs and FECs rise by 43% and 162%, respectively, compared to Case 0.

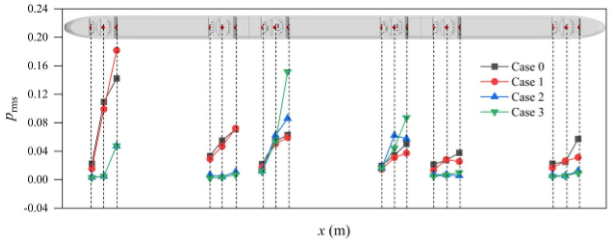

Fig. 20 RMS of fluctuating pressure in each bogie cabin

3.2.3 Analysis of OASPL of the bogie cabins

This section analyzes the overall sound pressure level (OASPL, L_{OA}) characteristics inside the bogie cabins of trains with different bogie covering configurations. The OASPL, a core index for evaluating the aerodynamic noise intensity of HSTs, is derived from the pressure fluctuations at each measurement point. The calculation formula is expressed as:

$$L_{OA} = 20\lg\left(\frac{p_{rms}}{p_{ref}}\right), \quad (3)$$

where P_{rms} is the RMS of the pressure fluctuation and P_{ref} is the reference pressure, adopted as 2×10^{-5} Pa in air. Fig. 21 illustrates the OASPL at internal measurement points to analyze the effects of bogie covers. The results show that the installation of covers significantly reduces the OASPL in the bogie cabins of the head and tail cars, with a reduction range of 10 dB to 25 dB. In contrast, the OASPL for the intermediate car exhibits an increase, although not exceeding 8 dB. This rise occurs because the sealing and flow-guiding effects of the covers result in a higher underbody flow velocity compared to Case 0 and Case 1. The higher-velocity flow directly impinges on the bogie structures of the middle car, thereby intensifying the radiated noise. The implementation of covers effectively blocks the direct impingement of high-speed shear flows, thereby significantly attenuating the strength of aerodynamic acoustic sources.

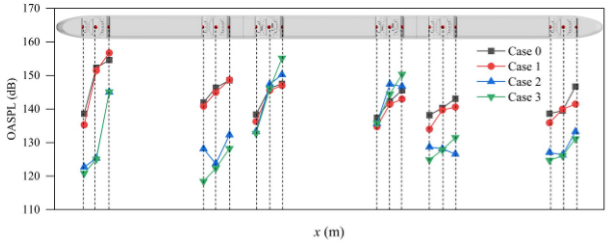

Fig. 21 Distribution of the OASPL in each bogie cabin

Fig. 22 presents the OASPL distribution on the lower surfaces of the covers. Specifically, Fig. 22a indicates that for the STC, the OASPL of Cover 1 is notably higher than that of the other three covers. The brake disc opening gap at its rear end, which serves as the main inlet for high-speed incoming flow into Bogie Cabin 1, exhibits the most intense pressure fluctuations and a maximum OASPL of 156 dB. Covers 2–4 have similar OASPL distributions, with peak values concentrated at the front brake disc opening gaps that are the main inlets for high-speed incoming flow into the corresponding bogie cabins. Fig. 22b illustrates that for FECs, the rear wheel opening gap of Cover 1, which acts as the primary inlet for high-speed incoming flow into Bogie Cabin 1, has a maximum OASPL of 160 dB, while its front wheel opening gap, the outlet for low-speed internal cabin airflow, has a minimum OASPL of 143 dB. Covers 2–4 also show similar OASPL distributions. As their front and rear wheel opening gaps serve as both airflow inlets and outlets, OASPL peaks are concentrated in these regions, with both front and rear peaks of Cover 2 exceeding 156 dB. While localized gaps in the head car cover exhibit relatively high OASPL due to airflow exchange, these high-acoustic-pressure regions are spatially confined. They do not induce broad-area, high-intensity vibration excitations across the entire cover; thus, their negative impact on the overall external noise radiation of the train is highly limited.

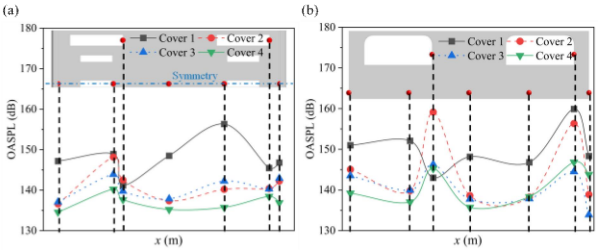

Fig. 22 Distribution of the OASPL on the lower surface of each bogie cover: (a) STCs; (b) FECs

4 Conclusions

This study used the improved delayed detached-eddy simulation (IDDES) method to investigate the aerodynamic characteristics of 1:8 scale high-speed train (HST) models at 400 km/h. The primary objective was to systematically explore how different bogie covering configurations, including separated-type covers (STCs), fully enclosed covers

(FECs), and skirts, affect the aerodynamic performance, lift fluctuations, underbody flow field, and overall sound pressure level (OASPL) of the train. The following conclusions are drawn:

1. All bogie covering structures effectively reduce the total aerodynamic drag of the train. FECs achieve the optimal reduction rate of 19.81%, followed by STCs (16.24%) and skirts (14.45%). Notably, while covers reduce drag on the head and tail cars, they slightly increase the drag of the middle car due to enhanced airflow impingement. FECs result in higher aerodynamic drag on the middle car compared to STCs.

2. The installation of skirts and covers significantly suppresses lift fluctuations on the car bodies, with STCs outperforming FECs. STCs reduce the RMS of lift coefficient fluctuations for the head, middle, and tail cars by 41%, 30%, and 44%, respectively, whereas FECs achieve reductions of 31%, 26%, and 37%. In terms of mean lift, STCs exhibit positive lift with lower fluctuation intensity, while FECs primarily show negative lift.

3. The dominant frequencies of lift fluctuations for STCs and FECs strictly align with the car body responses, characterized by a primary band at 7–14 Hz and a secondary peak at 63–72 Hz. As airflow passes through the bogie cabins, it triggers a cavity flow-induced resonance. This resonance couples the internal and external flows via the wheel gaps, generating dominant frequencies at approximately 10 Hz (first-order) and 65 Hz (fifth-order). This confirms that cavity flow-induced resonance is the core mechanism governing lift fluctuations.

4. Bogie covers significantly alter the pressure distribution and flow exchange within the bogie cabins. For the head and tail cars, the covers mitigate unsteady loads by blocking direct flow impingement; specifically, STCs and FECs reduce the pressure fluctuation RMS by up to 98% (head car) and 83% (tail car) compared to the baseline. Starkly contrasting this trend, in the middle car, covers exacerbate pressure fluctuations, with maximum increases reaching 43% for STCs and 162% for FECs. Regarding spectral characteristics, while covers generally suppress large-scale vortex shedding, boundary layer instability on the head bogie cover induces high-frequency flow field fluctuations (115–117 Hz). Conversely, the tail cover flow, characterized by fully developed turbulence, exhibits a much lower dominant frequency of approximately 10 Hz.

5. Bogie covers can reduce the OASPL in the bogie cabins of the head and tail cars by 10-25 dB by blocking the direct impact of airflow. However, they cause a slight increase in the OASPL of the middle car, with a maximum rise of 8 dB. High sound pressure levels on the covers are concentrated near geometric gap regions (e.g., wheel cuts and brake disc openings), where maximum values reach 160 dB (FECs) and 156 dB (STCs). These high-acoustic-pressure regions are spatially localized. They do not induce large-scale, high-intensity vibrational excitations across the entire cover; consequently, their adverse impact on the overall external noise radiation of the train is highly limited. Consequently, adopting the cover holds great promise for reducing the overall internal noise levels of the bogie cabin.

Overall, this study clarifies the interactions among bogie covering configurations, unsteady flow fields, and aerodynamic fluctuations, offering critical theoretical support for safety-oriented design. To prevent the detachment of bogie covers caused by flow-induced resonance, the natural frequencies of the covers and mountings must be strictly decoupled from the identified aerodynamic excitation bands (7–14 Hz, 63–72 Hz, and 115–117 Hz). Although the standard three-car consists provide a conservative evaluation of underbody aerodynamics, future research should explore full-length consists (e.g., 8- or 16-car).

Acknowledgments

The authors acknowledge the computing resources provided by the High-Performance Computing Public Platform of Central South University, China. The authors acknowledge the financial support provided by the National Key Laboratory of Advanced Technology for Cross-Domain Flight. This work was supported by the Science and Technology Research Program of China State Railway Group Co., Ltd. [Grant No. K2024J005-B(JB)]; the National Natural Science Foundation of China [Grant No. 52322215]; the National Natural Science Foundation of China-China State Railway Group Co., Ltd. Railway Fundamental Research Joint Fund [Grant No. U2368213]; the National Key R&D Program of China [Grant No. 2022YFB4301103]; National Natural Science Foundation of China [Grant No. U24B20123]; the Science and Technology Innovation Plan Project Program of Hunan Province, China [Grant No. 2024RC3016]; and the Natural Science Foundation of Hunan Province, China [Grant

No. 2025JJ50220, 2025JJ50017], the National Natural Science Foundation of China-Fundamental Science Center Project [Grant No. 52388102].

Author contributions

Hongkang LIU and Tiantian WANG designed the research. Jinning GONG and Kehui PENG processed the corresponding data. Jinning GONG wrote the first draft of the manuscript. Wenyue WANG, Yatian ZHAO and Zhenyu ZHANG helped to organize the manuscript. Jinning GONG revised and edited the final version.

Conflict of interest

No potential conflict of interest is reported by the author(s).

Declaration on the use of generative AI tools

No generative AI tools are used in the preparation of this manuscript.

Data availability

The data that support the findings of this study are available from the corresponding author upon reasonable request.

References

Baker CJ, 2016. A review of train aerodynamics part 1 – fundamentals. *The Aeronautical Journal*, 118(1201):201-228. https://doi.org/10.1017/s000192400000909x

Bell JR, Burton D, Thompson MC, et al., 2015. Moving model analysis of the slipstream and wake of a high-speed train. *Journal of Wind Engineering and Industrial Aerodynamics*, 136:127-137. https://doi.org/10.1016/j.jweia.2014.09.007

Dai Z, Li T, Zhang W, et al., 2024. Investigation on aerodynamic characteristics of high-speed trains with shields beneath bogies. *Journal of Wind Engineering and Industrial Aerodynamics*, 246 https://doi.org/10.1016/j.jweia.2024.105666

Dong T, Minelli G, Wang J, et al., 2020. The effect of reducing the underbody clearance on the aerodynamics of a high-speed train. *Journal of Wind Engineering and Industrial Aerodynamics*, 204 https://doi.org/10.1016/j.jweia.2020.104249

Dong T, Minelli G, Wang J, et al., 2022. Numerical investigation of a high-speed train underbody flows: Studying flow structures through large-eddy simulation and assessment of steady and unsteady reynolds-averaged navier–stokes and improved delayed detached eddy simulation performance. *Physics of Fluids*, 34(1) https://doi.org/10.1063/5.0075617

Gao G, Zhang Y, Miao X, et al., 2021. Influence of bogie fairing configurations on the snow accretion around bogie regions of a high-speed train under crosswind conditions. *Mechanics Based Design of Structures and Machines*, 51(10):5452-5469. https://doi.org/10.1080/15397734.2021.2003711

Guo H, Fu S, Liu J, 2024. Numerical and experimental study on the aerodynamic noise characteristics of 600-km/h high-speed maglev trains. *Transportation Safety and Environment*, 6(4) https://doi.org/10.1093/tse/tdae017

He Y, Thompson D, Hu Z, 2024. Aerodynamic noise from a high-speed train bogie with complex geometry under a leading car. *Journal of Wind Engineering and Industrial Aerodynamics*, 244 https://doi.org/10.1016/j.jweia.2023.105617

Heller HH, Holmes DG, Covert EE, 1971. Flow-induced pressure oscillations in shallow cavities. *Journal of Sound and Vibration*, 18(4):545-553. https://doi.org/10.1016/0022-460X(71)90105-2

Huang Z, Li W, Chen L, 2024. Effects of the reynolds number on train aerodynamics considering air compressibility: A wind tunnel study. *Transportation Safety and Environment*, 6(4):491-497. https://doi.org/10.1093/tse/tdae006

Kwon H, 2023. Characteristics of the air flow underneath high-speed trains running on the ballast track. *Journal of Wind Engineering and Industrial Aerodynamics*, 232 https://doi.org/10.1016/j.jweia.2022.105283

Li N, Li T, Dai Z, et al., 2024. Effect of streamlined nose length on aerodynamic performance of high-speed train with a speed of 400 km/h. *Journal of Zhejiang University-SCIENCE A*, 25(7):525-540. https://doi.org/10.1631/jzus.A2300301

Li R, Liu J, Qi Z, et al., 2011. Air pressure pulse developing regularity of high-speed trains crossing in open air. *Journal of Mechanical Engineering*, 47(04):125-130. https://doi.org/10.3901/JME.2011.04.125 (in Chinese)

Li W, Liu T, Zhou L, et al., 2023. Impact of ballast length on train aerodynamics for a wind tunnel layout via cfd analysis. *Alexandria Engineering Journal*, 65:275-293. https://doi.org/10.1016/j.aej.2022.10.040

Li Y, Li T, Zhang J, 2025. Mitigation of abnormal vibration on high-speed trains under unsteady aerodynamic loadings using bogie skirts. *Physics of Fluids*, 37(1) https://doi.org/10.1063/5.0244409

Liu W, Guo D, Zhang Z, et al., 2019. Effects of bogies on the wake flow of a high-speed train. *Applied Sciences*, 9(4) https://doi.org/10.3390/app9040759

Moon J, Kim S, Kwon H, 2014. A study on the aerodynamic drag reduction of high-speed train using bogie side fairing. *Journal of computational fluids engineering*, 19(1):41-46. https://doi.org/https://doi.org/10.6112/kscfe.2014.19.1.041

Muñoz-Paniagua J, García J, 2020. Aerodynamic drag optimization of a high-speed train. *Journal of Wind Engineering and Industrial Aerodynamics*, 204 https://doi.org/10.1016/j.jweia.2020.104215

Rossiter JE, 1962. The effects of cavities on the buffeting of

aircraft. Technical Report RAE Technical Memorandum No. Aero 754, Royal Aircraft Establishment, Farnborough, UK.

Shang W, Gao G, Miao X, et al., 2023. Impact of bogie fairing configuration on the aerodynamic performance of high-speed train under crosswind. *Mechanics Based Design of Structures and Machines*, 52(9):6209-6232. https://doi.org/10.1080/15397734.2023.2272686

Wang J, Gao G, Li X, et al., 2019. Effect of bogie fairings on the flow behaviours and aerodynamic performance of a high-speed train. *Vehicle System Dynamics*, 58(6):890-910. https://doi.org/10.1080/00423114.2019.1607400

Wang J, Minelli G, Dong T, et al., 2020. Impact of the bogies and cavities on the aerodynamic behaviour of a high-speed train. An iddes study. *Journal of Wind Engineering and Industrial Aerodynamics*, 207 https://doi.org/10.1016/j.jweia.2020.104406

Wang Y-N, Chen C-J, He H-Y, 2015. Large eddy simulation and wavelet decomposition for fluctuation pressure of high speed train. *Machinery Design & Manufacture*, (08):86-88+93. https://doi.org/10.19356/j.cnki.1001-3997.2015.08.023 (in Chinese)

Xia C, Shan X, Yang Z, 2016. Comparison of different ground simulation systems on the flow around a high-speed train. *Proceedings of the Institution of Mechanical Engineers, Part F: Journal of Rail and Rapid Transit*, 231(2):135-147. https://doi.org/10.1177/0954409715626191

Xiao Y-G, Zhang X-F, Kang Z-C, 2010. Large eddy simulation for fluctuation pressure of high speed train head surface. *Advanced Engineering Sciences*, 42(01):227-232. https://doi.org/10.15961/j.jsuese.2010.01.016 (in Chinese)

Zhang H, Shi G, Zhang X, et al., 2019. Research on the control of wheel-rail noise by wheel sound-proof skirt for high-speed train. *2019 IEEE International Conference on Mechatronics and Automation (ICMA)*, :2064-2069. https://doi.org/10.1109/ICMA.2019.8816428

Zhang J, Li J-J, Tian H-Q, et al., 2016. Impact of ground and wheel boundary conditions on numerical simulation of the high-speed train aerodynamic performance. *Journal of Fluids and Structures*, 61:249-261. https://doi.org/10.1016/j.jfluidstructs.2015.10.006

Zhang J, Wang J, Wang Q, et al., 2018. A study of the influence of bogie cut outs' angles on the aerodynamic performance of a high-speed train. *Journal of Wind Engineering and Industrial Aerodynamics*, 175:153-168. https://doi.org/10.1016/j.jweia.2018.01.041

Zhang J, Adamu A, Su X-C, et al., 2022. Effect of simplifying bogie regions on aerodynamic performance of high-speed train. *Journal of Central South University*, 29(5):1717-1734. https://doi.org/10.1007/s11771-022-4948-2

Zhao C, Wang T, Zhou G, et al., 2025. Wind tunnel experimental investigation on the performance of the ice-melting system for high-speed train bogies. *Transportation Safety and Environment*, 7(1) https://doi.org/10.1093/tse/tdae022

Zheng X-H, Zhang J-Y, Zhang W-H, 2011. Numerical simulation of aerodynamic drag for high-speed train bogie. *Journal of Traffic and Transportation Engineering*, 11(02):45-51. https://doi.org/10.19818/j.cnki.1671-1637.2011.02.008

Zhou P, Li T, Zhao C-F, et al., 2020. Numerical study on the flow field characteristics of the new high-speed maglev train in open air. *Journal of Zhejiang University-SCIENCE A*, 21(5):366-381. https://doi.org/10.1631/jzus.A1900412

Electronic supplementary materials

Section S1–S8, Table S1, Figs. S1–S3, Eqs. S1–S6